[American Journal of Science, Vol. 313, April, 2013, P. 326–344, DOI 10.2475/04.2013.03]

MOUNTAIN-BUILDING UNDER EXTENSION

TILL SACHAU*,†, DANIEL KOEHN**, and CEES PASSCHIER*

ABSTRACT. A mechanism is presented which explains how intra-continental rifting can cause large topographic uplift. The effect is sufficient to account for the uplift of rift flanks and the very high and strongly localized uplift of the Rwenzori horst in the Western Branch of the East African Rift System. We propose that the uplift is generated by crustal bending, which is caused by a misfit of the lateral tensile stress between the upper and middle crust. The misfit is a function of different yield mechanisms when the upper crust breaks whereas the middle crust flows.

Two independent numerical schemes confirm the suggested uplift mechanism. Both models—a 2 and 2.5 D elastoplastic lattice-particle model and a multilayer beam model—were used to calculate the surface topography as a result of lateral uniaxial extension. Using the fault geometry of the Rwenzori area, we find that the amount of topographic uplift is controlled by the viscosity and elasticity of the crust. The extreme uplift of the Rwenzori horst is—at least to some extent—a function of its considerably high elastic stiffness. The stiffness unites the two rifts that bound the Rwenzori horst and leads to an extremely high topography and a high Moho uplift in the center of the two rifts where the Rwenzori mountains sit.

Key words: Horst uplift mechanism, rift flank uplift, crustal bending, Rwenzori, rift transfer zone, numerical model

INTRODUCTION

The primary motivation of this numerical study was to determine the mechanism that caused the very high uplift of the Rwenzori Mountain Range, a problem that has long been a puzzle for geologists (Bahat and Paul, 1987; Ebinger, 1989; Karner and others, 2000; Chorowicz, 2005; Wallner and Schmeling, 2010). Until now, the problem is without a final solution. The Rwenzori Mountains are the highest non-volcanic mountains in Africa with a maximum elevation of 5109 m (fig. 1A), and are located in a rift-transfer zone within the Western Branch of the East African Rift System (Koehn and others, 2008; Link and others, 2010). The Rwenzori represent a large horst with major boundary faults that are located between the Semliki and the Lake George rift segments (Upcott and others, 1996; Karner and others, 2000; Ring, 2008).

The Rwenzori Mountains are situated within a rift zone and are therefore located in a region of crustal thinning. Commonly, such a tectonic setting results in the creation of deep rift valleys, not in mountain building (Buck, 1988). However, the Rwenzoris are almost 4000 m above the continental plateau, and 3000 m above the rift flanks (fig. 1B). Horst uplift may occur within an extensional setting as is the case in the Basin-and-Range Province in the western USA (Buck, 1988, 1991; Parsons, 2006), however, this uplift is not as extreme as in the Rwenzori case.

Even though crustal thinning is a substantial part of rift formation (Gölke and Mechie, 1994), topographic upheaval of the rift flanks is a common phenomenon. As this type of uplift will play an essential role in the ensuing discussion, a short description of existing models follows.

Many explanations for rift flank uplift are based on isostatic rebound (Royden and Keen, 1980; Kusznir and Ziegler, 1992; Karner and others, 2000). If unstretched lithosphere is in isostatic equilibrium, crust that is actively stretched may be subjected to isostatic uplift or subsidence. The type of vertical movement will depend on the

* Institut fuer Geowissenschaften, Tectonophysics, University of Mainz, Mainz, Germany
** School of Geographical and Earth Sciences, University of Glasgow, Glasgow, United Kingdom.
† Corresponding author: sachau@uni-mainz.de

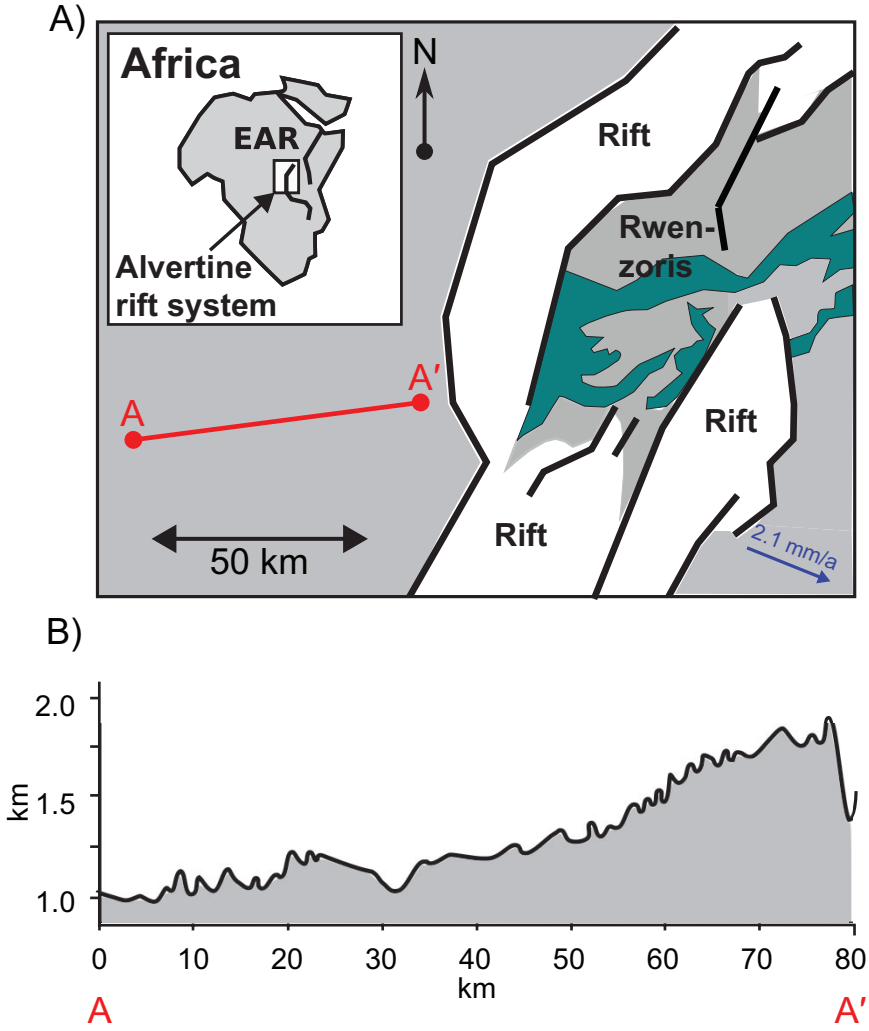

Fig. 1. (A) Simplified geological map of the Rwenzori area (after Link and others, 2010). Gray units represent gneisses of the Gneissic Granulite Complex and sandstones, conglomerates and argillaceous sediments of the Kibaran Belt. Green units represent the Buganda-Toro Belt, consisting mainly of schists, amphibolites, quartzites. Black lines are major boundary faults of the rifts and the Rwenzori horst. The red line from A to A′ marks the topographic profile displayed in (B).

weight of the lithospheric column before and after stretching (McKenzie, 1978). For instance, Karner and others (2000) describe a model where crustal load is removed along a listric fault transecting the lithosphere, which leads to uplift of the footwall of the fault. This model has been successfully applied to rift flank uplift within the Albertine Rift System (Karner and others, 2000). Karner and others (2000) also argue that the extreme height of the Rwenzori horst may have resulted from the combined uplift effect of the two rift segments that flank it. However, there is no indication for crustal listric faults in the existing seismic data (Lindenfeld and others, 2012; fig. 2A). Also the gravity map below and east of Lake George rift does not indicate a major basin, as required by the Karner and others (2000) model.

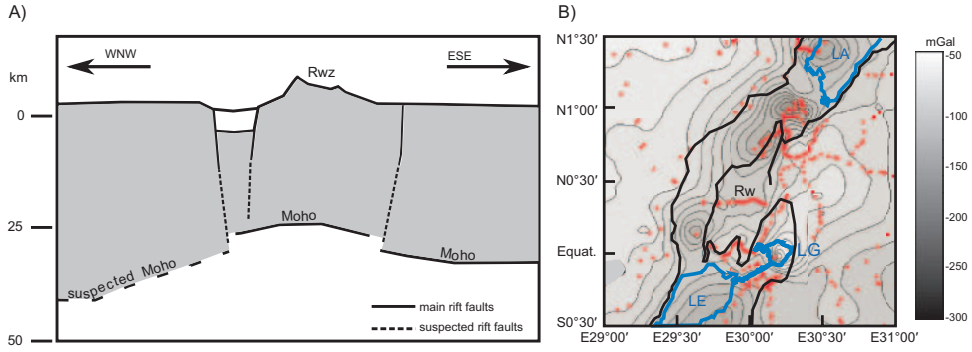

Fig. 2. (A) Sketch of the Moho and of the main rift faults in the Rwenzori region. After a cartoon of Lindenfeld and others (2012), who compiled seismic data from Wölbern and others (2010) and Wölbern and others (2012). Arrows indicate the orientation of the crustal profile and of the approximate rift opening. (B) Bouguer gravity anomaly map, generated from data of the Bureau Gravimétrique International (BGI). Interpolation uses the Kriging method. LA = Lake Albert, LE = Lake Edward, LG = Lake George, RW = Rwenzori Mountains. Red dots indicate where gravity measurements were taken.

In a more complex numerical setup, Kusznir and Ziegler (1992) present a model where rift flank uplift is produced by the kantilever effect. Again, material is taken off locally along a listric fault leading to isostatic rift flank uplift in the footwall of the fault. Kusznir and Ziegler (1992) do not only show the kantilever effect elevating rift flanks but they also show a horst that is subject to uplift because of kantilever effects on its bounding faults. However, the horst presented in the numerical model of Kusznir and Ziegler (1992) is not higher than the rift flanks and shows a Moho depression below the horst. Recent seismological data shows that the Moho is high below the Rwenzori horst (Lindenfeld and others, 2012; fig. 2A). In summary, the kantilever effect can lead to horst uplift, however the uplift is not as extreme as it is in the Rwenzori case and the seismological data does not support this mechanism.

An alternative process to the localized rift flank uplift that is known to produce uplift in regions associated to rifting is thermal doming. However, the length scale of such domes is in the range of 500 to 1000 m (Morley and others, 1990), and is thus too large to account for the very localized uplift of the Rwenzori horst. In addition, thermal doming is not known to produce the very high elevation, which is necessary to explain the Rwenzori mountain range.

Wallner and Schmeling (2010) presented a model for the Rwenzori uplift based on lithospheric mantle delamination. The main idea is that the lower mantle lithosphere is replaced by lighter asthenospheric material that leads to an isostatic uplift. Mantle delamination is known to produce uplift across large areas, whereas it was never shown to result in the uplift of small blocks like the Rwenzori horst. The model of Wallner and Schmeling (2010) is based on the assumption that the extension below the Semliki and George rift is so localized that a small block of lithosphere below the Rwenzori horst can detach from the lower crust and the horst is then subject to isostatic uplift. The main problem with this model is the absence of seismic events below the Rwenzori horst, which one would expect if a large volume of brittle lithosphere is delaminated below the horst. In addition the gravity map of the Albertine rift shows no significant gravity low below the Rwenzori horst, a feature that would be expected during very localized delamination (fig. 2B).

So how does one explain the very high Rwenzori mountains? In this article we propose a mechanism, which is able to function as an additional driving force for the

horst uplift. The mechanism was derived and tested using two different numerical models. Our models are not based on a single elastic beam but model lithospheric extension with multilayer models that have visco-elasto-plastic properties so that the layers can contain strain gradients and may act more viscous or more brittle depending on boundary conditions. Firstly, an elastoplastic 2D lattice-particle model was developed and used to calculate 2D-sections through mantle and crust during the rift opening. The numerical scheme considers dynamic fault development, the regional geology and the layered properties of the lithosphere. Based on the numerical model we derived a new uplift mechanism, which is able to contribute significantly to the Rwenzori uplift.

The mechanism causes and explains the associated phenomenon of rift flank uplift as well, which allowed us to test the basic assumptions of our hypothesis in a simplified setting. For this purpose an additional numerical model was developed, which is directly based on equations governing the proposed mechanism. This second model does not take horst uplift into account, but restricts itself to a crustal section affected by rift flank uplift. These additional simulations are meant to test and confirm the viability of the mechanism within a physically reasonable range of material parameters.

GEOLOGY OF THE RWENZORI AREA

The Rwenzori Mountains comprise a horst with a length of 120 km, a maximum width of 50 km, and an elevation of more than 5100 m (Bahat and Paul, 1987; Koehn and others, 2008; Ring, 2008). It is located in the northern part of the western branch of the East African Rift System, known as the Albertine rift system (fig. 1). It is situated at a node where two rift segments are connected. The northern segment is thought to have nucleated in the vicinity of Lake Albert and the southern segment near Lake Edwards (Morley and others, 1990). The rift nuclei are thought to have protruded towards each other and captured the Rwenzori basement block, which now serves as a transfer and accommodation zone (Koehn and others, 2008, 2010). Block capturing of the Rwenzori-type is known from other locations within the East African Rift Valley (Bahat and Paul, 1987). Examples include the Amaro Horst in Ethiopia, which is uplifted about 1.5 km above the graben floor (Wolde Gabriel and others, 1991) and the Mbeya Mountains in Tanzania, which have an elevation of up to 2900 m.

Continental extension is localized in the 40 to 70 km wide Albertine rift basins, accommodating a total crustal extension of about 10 km according to estimates of (Ebinger, 1989). Gravity data of the Geological Survey of Uganda and Upcott and others (1996) indicate that the Semliki rift, that is situated west of the Rwenzoris, is much deeper with a significant negative anomaly in contrast to the eastern lake George rift that does not show a strong anomaly and is thought to be only about 2 km deep (Upcott and others, 1996; fig. 2B). In addition, the Lake George rift stops in the northern part of the Rwenzori where the horst is still connected to the eastern Victoria plate. It is thought that the onset of rifting occurred at around 10 to 12 Ma (Ebinger and others, 1989; Pickford and others, 1993), and a first major rifting episode has been proposed to have occurred at about 7 to 8 Ma ago (Pickford and others, 1993). Activity in the Albertine Rift is thought to have increased about 2.6 Ma ago, including increased uplift of the Rwenzori Mountains and rifting (Schlueter, 1997; Bauer and others, 2010, 2012; Roller and others, 2010). The current opening rate of the rift amounts to 2.1 mm/a in the Rwenzori region, according to recent GPS measurement (Stamps and others, 2008).

The seismological research of Lindenfeld and Rümpker (2011) shows that seismic activity in the west of the Rwenzori mountains ranges from 10 to 20 km deep. In the east of the Rwenzoris, where they are still connected to the rift shoulders, seismicity extends from the surface down to 30 km depth. Brittle faulting seems to concentrate

on the main boundary faults of the horst (Koehn and others, 2008; Ring, 2008; Sachau and Koehn, 2010), which is manifest in the location of the clustering of earthquake epicenters along the proposed major faults (Koehn and others, 2010; Lindenfeld and others, 2012). Seismic activity below 16 km depth outside the rift is almost nonexistent except for the area where the Rwenzori horst is connected to the Victoria plate (Lindenfeld and others, 2012), where a few extremely deep earthquakes have been measured. The Moho depth in the Rwenzori region is generally in the range of normal continental crust with depths of 30 km and more below the eastern rift shoulder (Wölbern and others, 2010; Lindenfeld and Rümpker, 2011). Directly below the Rwenzori horst, however, it is uplifted to a depth of 21 km (Wölbern and others, 2010). Figure 2A shows a sketch of the Moho beneath the Rwenzori region (after Lindenfeld and others, 2012).

It is interesting to note that the Bouguer gravity anomaly beneath the Rwenzori Mountains [fig. 2B shows a Bouguer gravity map based on data of the Bureau Gravimétrique International (BGI)] is basically flat, which is in contradiction to the elevated Moho predicted by the seismological data.

The basement geology in the Rwenzori area is relatively unusual for the East African Rift System. Most young rifts tend to follow weak mobile belts of Proterozoic age and surround Archean cratons. In the Rwenzori area, however, the rifts cross a Proterozoic fold-and-thrust belt (Link and others, 2010) and enter the Archaen Congo Craton towards the north. The Rwenzori fold-and-thrust belt is mainly made up of amphibolite, shist and quartzite (fig. 1A) that are thrusted northwards onto the Archean craton. The belt itself seems to resemble thick-skinned tectonics where relatively thick thrust slices composed of Proterozoic volcanics and sediments and Archaen basement are stacked (Link and others, 2010). The thrust slices dip towards the South at roughly 50 to 60° and the boundaries cross the Rwenzori horst. This geometry makes the horst relatively stiff, especially around a thick amphibolite slice that sits in the center of the high mountains and defines the high peaks of Magerita (+5100 m) and Baker (+4800 m). A second important geological basement feature is the existence of vertical mylonite zones that trend SSW-NNE and SSE-NNW, crosscutting the older fold and thrust belt (in particular the Nyamwamba fault), (McConnell, 1972; Link and others, 2010; Bauer and others, 2012). These features have two effects. They make the internal horst stronger because brittle faulting is localized in the old shear zones and they also make the brittle faults very steep and localized. It is thought that some of these faults are reactivated during the young brittle uplift (Koehn and others, 2008; Ring, 2008; Link and others, 2010).

The mechanical properties of the lithologies making up the Rwenzori horst differ considerably from those comprising the surrounding area. The elastic modulus and the tensile and compressive strength of amphibolites and quartzites are approximately twice those of gneisses and sediments (Palmström and Singh, 2001; Cai, 2009). The Rwenzoris thus form a rigid block within a comparatively weak matrix.

Magnetotelluric observations suggest the presence of an electrical anisotropy below the Rwenzori horst (Häuserer, 2010). This observation can be explained by the presence of oriented olivine due to an elevated Moho, if the Moho was subjected to a stress field perpendicular to the rift axis.

PROPOSED UPLIFT MECHANISM

We propose the hypothesis, that the Rwenzori block is uplifted by a mechanism that is based on similar principles as the uplift mechanism for rift flanks described in Sachau and Koehn (2010) and Sachau and others (2011).

The mechanism relies on the specific response of the lithosphere to an externally applied tensile stress. Lateral tension in the brittle-elastic uppermost crust will result in instantaneous and time-independent stress or in brittle failure. In the ductile region

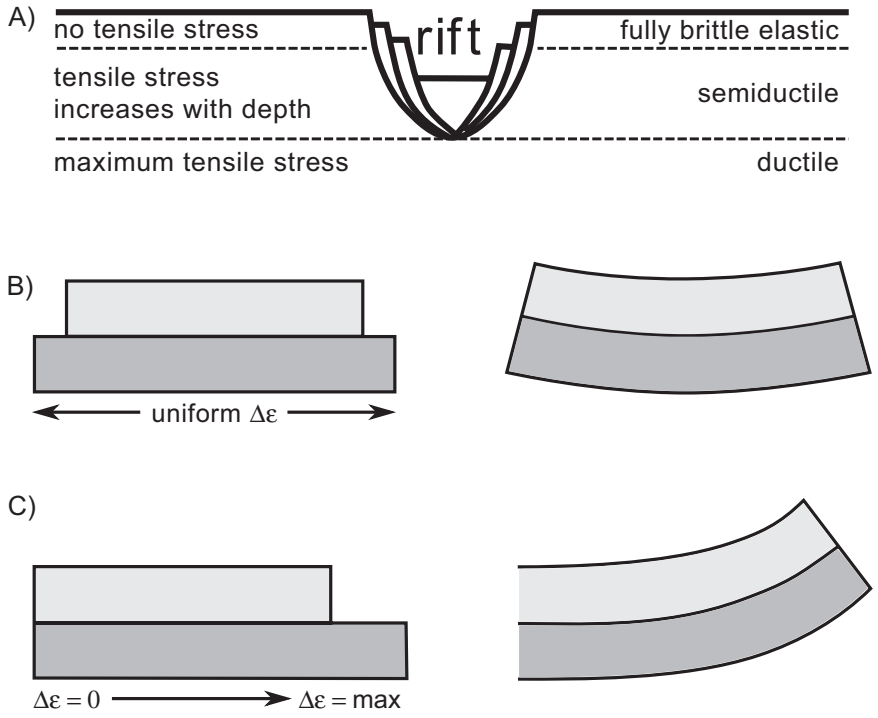

Fig. 3. Illustration of the beam model. (A) Simplified section through the crust in a rift region. The uppermost crust is brittle, tensile stress is instantaneously and completely released by brittle failure. The semi-ductile layer below compensates stress partly by brittle failure and partly by ductile yielding. Tensile stress increases with depth, due to the increasing ductility. In the fully ductile layer below tensile stress is almost homogeneously distributed and tensile stress below the rift is at its maximum. (B) General case of the generation of curvature in a flat plate, caused by a uniform misfit strain $\Delta\epsilon$ between two bonded layers. (C) The misfit strain $\Delta\epsilon$ between the layers is 0 at the left, and increases steadily to the right. As a result, curvature increases from left to right.

between middle crust and upper mantle the lateral tensile stress will decay with time. The ductile stress decay will amplify the tensile stress in the uppermost brittle crust, where it will initialize or increases the rate of brittle failure, which will further increase the stress in the crust [see fig. 3A and compare Kusznir and Park (1982)].

Within the EARS, brittle failure of the lithosphere will be localized at the main rift faults (Chorowicz, 2005). The type of feedback mechanism described above leads to the increase of the tensile stress from the topmost brittle layers towards the brittle ductile transition, below which no more brittle failure occurs. Due to the strong localization of brittle failure in the EARS, the vertical stress difference is most significant in the immediate rift vicinity (fig. 1).

Assuming that the various layers of the lithosphere are welded to one another, the vertical increase of the tensile stress produces an upwards-directed bending moment within the lithosphere [fig. 3B; Clyne (1996)], an effect that is well known from beam bending in elastic theory (Sadd, 2005). The intensity of the effect increases with proximity to the rift, which is in agreement with the topography known from rift flanks (fig. 3B and fig. 4).

If we apply this mechanism to the Rwenzori mountains we have to take the local geology into account. The Rwenzori transfer zone consists of the stiff Rwenzori block, which comprises stacked amphibolitic and slaty rocks with an estimated thickness of 20 km

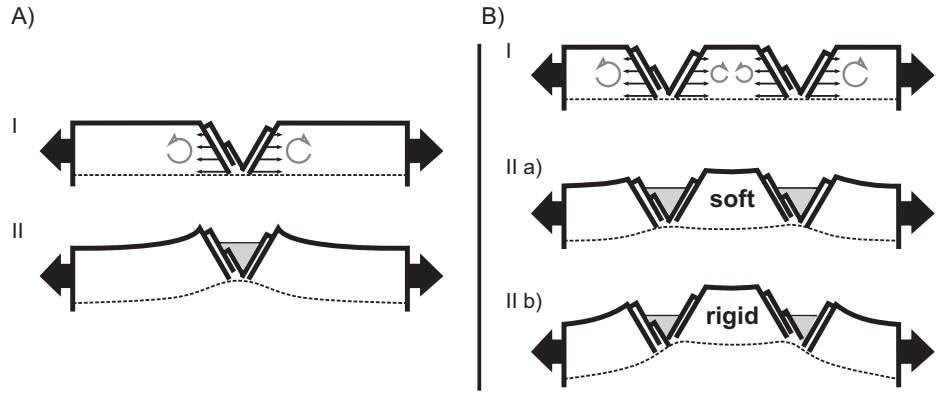

Fig. 4. Two sections through extended crust, with rift graben. Left column (A): curvature increases towards the rift-faults (rift flanks), as a result of the tensile stress difference between layers close to the surface and layers close to the base of the rift faults. Right column (B): two parallel rift segments generate ordinary rift flanks at the far left and the far right. Uplift of the horst block in between the rift segments is even larger than uplift of the rift flanks (II a). If the horst block is more rigid than the surrounding crust, horst uplift is amplified by the higher curvature at the transition from the rift flank to the horst (II b).

(Link and others, 2010). The block is bounded on each side by two parallel rift segments and has a width of about 30 km. The Moho beneath the Rwenzori block has a minimum depth of about 21 km (Wölbern and others, 2010).

The large elastic stiffness of the block and the underlying mantle material further increases the lithospheric upward flexure in vicinity of the rift and forms a bridge between the opposing rift segments. Both effects amplify the uplift of the Rwenzori block (fig. 4). We propose the hypothesis that the bending effect of a layered crust in combination with the stiffness of the Rwenzoris leads to block uplift and elevation of the Moho below the block.

The mechanism shares an important precondition with many other models, by requiring a layered crust consisting of an upper brittle and a lower ductile region (Bott, 1976; McKenzie, 1978; Buck, 1988; Kusznir and others, 1991). However, the driving forces behind previous models are either isostatic uplift or lateral displacement of mantle material, both mechanisms triggered by tectonic processes primarily in the brittle crust. In contrast, the driving force that we propose is a pure bending moment in the (semi-)brittle lithosphere, whose uplift effects might be amplified or opposed by isostatic effects or by the flow of mantle or lower crustal material.

NUMERICAL TESTS

We performed two different types of numerical experiments to test our hypothesis. The first part of these experiments consisted of 2 and 2.5 dimensional viscoelastic-plastic lattice-particle simulations with dynamic fault formation with different software packages. Both models have specific advantages and disadvantages, discussed below. In these experiments we evaluated the role of the crustal rheology on uplift.

The second part of the numerical experiments consisted of an explicit forward model of two bonded layers, both suffering different degrees of extension. This second type of numerical modeling was necessary to confirm the viability of the proposed uplift mechanism in a clean setup, without the possibility of unintentional 2D or 3D effects, which may occur in lattice particle simulations.

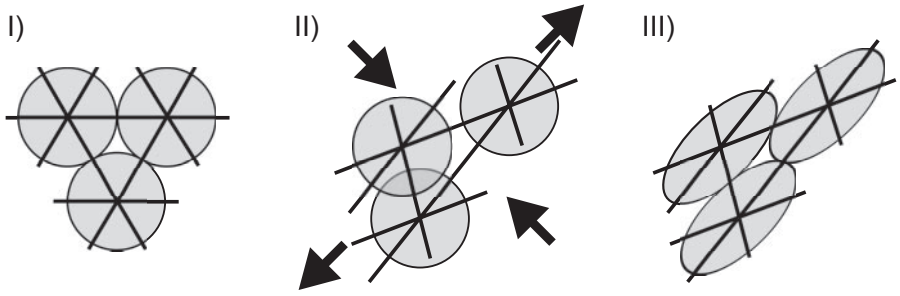

Fig. 5. Sketch of the viscoelastic deformation of particles and of the spring network for the 2D triangular next-neighbor lattice. Circles/ellipses represent particles, which also define the equilibrium length of springs. I) Circular particles prior to deformation. II) Application of external strain, indicated by the arrows, results in a new lattice configuration and in compressive and tensile stresses where particles overlap or are torn apart. III) Time dependent viscoelastic deformation results in elliptical particles. Depicted is the fully relaxed state at $t \to \infty$. Particle deformation is volume conservative.

LATTICE-PARTICLE SIMULATIONS

Software

The lattice-particle experiments were calculated in 2D and 2.5D, using the software-packages "Latte" (Koehn and others, 2006), and "Melange" (Sachau and Koehn, 2012). Both software packages are capable of modeling viscoelastic-plastic materials. Below we give a short description of the basic principles behind lattice-particle models. Comprehensive descriptions of the software packages are given in Koehn and others (2006) and Sachau and Koehn (2012).

Both "Latte" and "Melange" employ regular elastic spring lattices. "Latte" uses a 2D triangular spring network, while "Melange" employs a 3D hexagonal close-packed next-neighbor spring lattice. Discrete circular or spherical elements, termed "particles," are superposed on the nodes of the respective spring network.

The force acting on a lattice-node is calculated from the relative position of the connected neighbor nodes and from the repulsion of unconnected particles. An over-relaxation technique is employed (Allen, 1954) in order to calculate a configuration, where all nodes are in a state of force equilibrium. Such a reconfiguration has to occur whenever an external strain is applied to the system or—in case ductile plasticity is considered—after every time step.

A full stress tensor is calculated for every particle and/or node. Viscoelastic plasticity is modeled as the time-dependent, permanent and volume conservative deformation of particles and the local lattice geometry, controlled by the local deviatoric stress tensor (fig. 5). Gravity is simulated by assigning a scaled vertical weight force to each individual particle.

Both software-packages have their own advantages and disadvantages. The 2D "Latte" experiments are computationally less expensive than experiments with "Melange." "Latte" is therefore the preferred software in numerical experiments where dynamic fault formation is involved. Faults develop whenever the tensile stress on a spring exceeds a predefined yield value, upon which the spring in question is removed from the network. After a spring between two nodes is removed, the repulsion between the particles attached to the nodes is the only remaining force.

The software "Latte" does not consider the shear force acting on a spring between connected nodes but is restricted to normal forces. This is a common restriction of many lattice codes but as a consequence "Latte" does not consider shear failure of springs. The software "Melange," in contrast, considers both shear and normal forces between nodes as well as shear and tensile failure of springs.

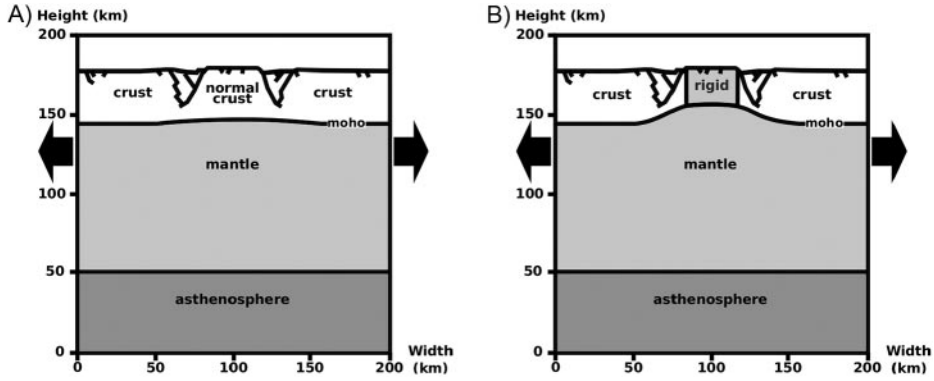

Fig. 6. Setup of the 2D hybrid lattice-particle model. The figure displays the section through lithosphere and asthenosphere used in the model, black arrows indicate the direction of crustal extension. The location of horst and rift faults is indicated. (A) uses a flat Moho and a Rwenzori horst with the same strength as the surrounding crust. (B) shows a setup with elevated Moho below the Rwenzori horst. The horst itself is more rigid than the surrounding crust, due to its geological composition.

Setup

The lattice-particle simulations consist of simplified vertical sections through the crust and the upper mantle. The crustal structure reflects the layer-wise increase of stiffness, strength and viscosity, known to occur in the lithosphere (Gölke and Mechie, 1994) and is shown in figure 6 and table 1. The crustal thickness is 35 km, the thickness of the upper mantle is 100 km and the lower part of the model consists of a 40 km thick slice of asthenosphere.

Simulations end after 5 million model years. At this point the system is stretched up to 10 km, equivalent to a constant opening rate of 2 mm/y. Stretching of the mantle is homogeneous. Crustal stretching, in contrast, occurs localized in the areas of the later rift segments. Localized crustal stretching is achieved by discrete block movements of the central 40 km wide proto-horst and rift flanks. The blocks are separated by 30 km wide regions where the strain is localized and where rift related normal faulting is triggered.

Real geological systems are characterized by their inherent disorder, local deviations from the idealized conditions of the numerical setup (Malthe-Sørenssen and others, 1998). These random influences are considered in the numerical simulations

Table 1

Viscosity, density, and Young's modulus of crustal rheological layers as used in the hybrid lattice-particle simulations

Depth (km)	0-25	25-35	35-140	140-200
Elastic modulus (10^{11} Pa)	0.85	1.08	1.8	1.8
Density (kg/m^3)	2750	2900	3200	2900

Depth (km)	0-8	8-25	25-30	30-35	35-40	40-50	50-60	60-140	140-200
Viscosity (10^{21} Pa s)	105	100	2	0.1	0.2	0.5	1	0.2	1

Compiled from Gölke and Mechie (1994), Li and others (2009), and Behr and Platt (2011).

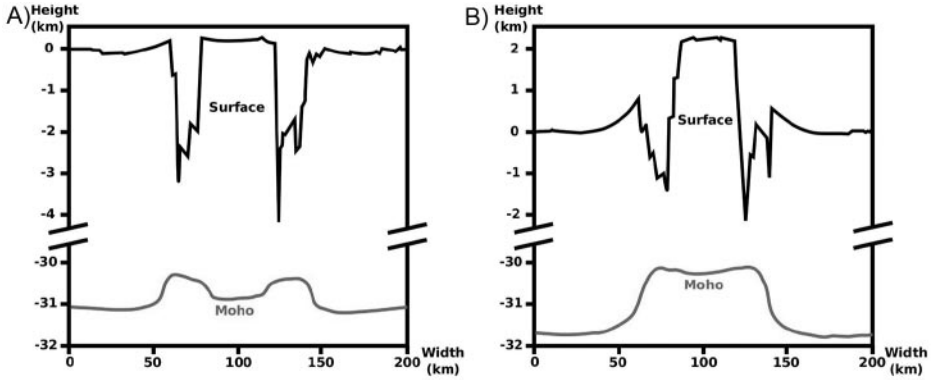

Fig. 7. Surface and moho uplift resulting from the lattice-particle model at 10 km total crustal extension. (A) displays the situation where the stiffness of the central block equals the stiffness of the surrounding crust. In (B), the stiffness of the central horst is twice that of the surrounding crust. The reference elevation ("0 m") is defined by the basis of the rift flanks.

by putting a Gaussian quenched noise on the elastic modulus and tensile strength of the mechanical springs.

The 2.5D setup that we use with "Melange" consists of a numerically 3 dimensional, yet very thin vertical section. The boundary conditions—uniaxial strain rate, rheological parameters and the height of the model (100 km)—are identical with the 2D experiments. The model width is 200 km. The model employs periodic boundaries in Z-direction and fixed boundaries in X-direction (Sachau and Koehn, 2012).

Experiments and Results

Horst uplift with dynamic faulting and viscoelastic lithosphere.—We modeled an experimental series where the stiffness of the central horst was gradually increased. Endmembers of the experiment series were a horst with normal crustal strength and stiffness, and a horst with twice the strength and stiffness as the surrounding crust that approximates the probable situation in the Rwenzori area. Experiments were performed in 2D using the software "Latte."

Extension of homogeneous crust.—In the first simulation the crust is homogeneous, assuming that the local geology is not essential for the formation of active rifts and the horst uplift (fig. 6A). The topography of the model surface (fig. 7A) shows that two rifts develop with rift flanks reaching 500 m maximum, a central horst with 600 m uplift and basins with up to 4000 m depth. Faults that develop in the model have a dip of about 65 degrees and do not propagate into the viscous lower crust. The horst shows approximately the same uplift as the main rift flanks and is subjected to bending, so that it develops two rift flanks and a central depression itself. The reference value for these heights is the elevation of the rift flanks where they show the least uplift.

The Moho, representing the boundary between crust and mantle, shows a similar geometry. The Moho-uplift is about 900 m below the two rifts, and about 200 m below the horst. Crustal thinning in this model is thus concentrated to the two rifts, whereas the horst is only thinned by a small amount.

Extension of crust with a stiff central block.—In the second simulation we considered the specifics of the Rwenzori geology by making the central block twice as stiff as the surrounding crust (fig. 6B). This mimics two geological and geophysical observations: firstly, that the horst consists of a stiff material and the Moho is very shallow at ~21 km depth. Secondly, that the horst is bound by vertical shear zones that place stiff units next to non-stiff units (see Link and others, 2010 and map in fig. 1A).

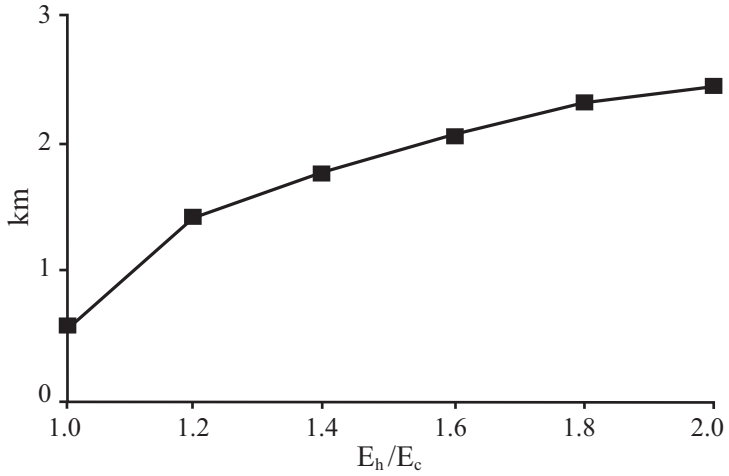

Fig. 8. Uplift of the central horst as a function of its elastic stiffness. The figure plots the ratio of the horst stiffness and the stiffness of the surrounding crust (E_h/E_c), against the resulting horst uplift. E_c = 0.85×10^{11} Pa. The curve appears to be near-linear in the range from 1.2 to 1.8, but shows overall convergence against some maximum uplift.

The topography resulting from this simulation (fig. 7B) shows two rifts with rift flanks and a central horst, which reaches approximately 2400 m above the continental plateau. The rigidity of the horst resists bending forces, thus the horst does not develop rift flanks. The Moho uplift is high compared to a homogeneous crust, and is not restricted to the areas below rifts. The amount of uplift is about 1700 m below rifts, and is still about 1500 m below the horst. The rift basins are also affected, they are shallower than in the first simulation and reach a depth of 2500 m. Crustal thinning occurs in a unified zone below the two rifts and the horst.

In a set of systematic modifications to these experiments we varied the rigidity of the central horst relative to the surrounding crust from 1.0, 1.2, 1.4, 1.6, 1.8 to 2.0, here expressed as the ratio of the stiffness of the horst relative to that of the crust. Within this range of values the resulting uplift of the central horst follows a non-linear trend, from 600 m uplift if the ratio of the stiffness of crust to horst is 1, to 2400 m when the horst is twice as stiff as the crust. With increasing horst stiffness the further increase of the uplift of the central horst slows and appears to converge to a limit (fig. 8).

Fault localization with shear forces and shear failure.—In a second simulation set we modeled the localization of fractures in the lithosphere when shear failure and shear forces between nodes are considered. These simulations were necessary in order to validate the localization of fractures in the previously discussed simulations, which were restricted to tensile failure. For these experiments we used the software "Melange" with a 2.5D setup.

Figure 9 shows the rheology and the setup of the model, where a viscoelastic mantle and lower crust and an elastic upper crust was used. The elevated Moho in the center of the model has a width of 35 km and the model uses a Mohr-Coulomb law to determine spring failure, which relates the shear strength of a spring to the normal stress and the angle of internal friction by

$$\tau_{crit} = c - \sigma_n \tan \Phi, \tag{1}$$

where $\Phi = \pi/6$ is the angle of internal friction. The tensile strength is 40 MPa, and the cohesion (c) can be derived from the tensile strength and the angle of internal friction

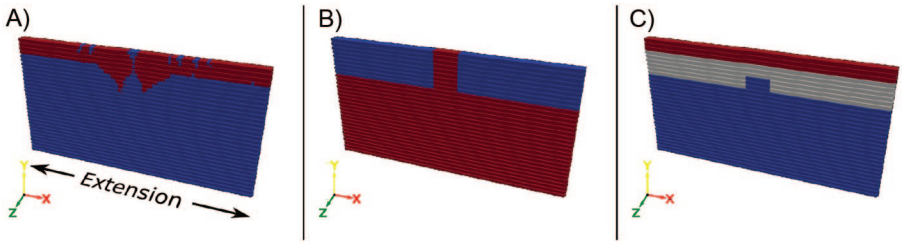

Fig. 9. Distribution of crustal faulting in the 3D HCP model with shear interactions and shear breaking ("Melange"). The setup of the profile—a thin slice through the crust—makes the model effectively 2.5 D. (A): two deep rooted fault zones—the later rift grabens—develop at both sides of the horst. (B): Young's modulus. (C): viscosity. Values of the viscosity and the Young's modulus are similar to the 2D model (table 1).

(Jiang and Xie, 2011). The natural inherent disorder of the material was modeled with a Gaussian normal distribution (standard deviation $\sigma = 0.05$) on the Young's modulus of springs.

Under extension the model develops pronounced deep rooted fracture zones (fig. 9), which surround the central block and are in a region where rifts would be expected at a later stage of the extension. The tips of these fault zones reach a depth of 30 km, and the width of the rifts is 25 to 30 km. These values are similar to the width of rifts in the Rwenzori region, and to the rifts in the 2D experiments (fig. 7).

BEAM BENDING MODEL

In order to test the beam-bending hypothesis with a less complicated model, we developed an explicit numerical forward model, which calculates the amount of uplift caused by two bonded crustal layers with different extensions (fig. 10). This model can only be used to study uplift of one rift flank, or the bending of one side of the Rwenzori horst. The original layered beam bending equations derived by Clyne (1996) consider purely elastic layers, therefore we replaced the Young's modulus E with the viscoelastic relaxation modulus E_{rel}, the time-dependent equivalent to E. See Appendix A for details about numerical assumptions and derivation of the governing equations.

Setup

The model applies incremental lateral uniaxial tension, until a total extension of 10 km is reached. The extension rate is 2 mm/a and the total model time is 5 Ma.

The depth of the main boundary fault is assumed to be 25 km, as indicated by recent seismological data (Lindenfeld and Rümpker, 2011). The layer thickness for both model layers is 12.5 km, equivalent to half the fault height. Viscosity and elastic modulus of both layers are adapted to values that can be expected in the crust (see experiment section below). The profile length is 80 km in accordance with the topographic profile displayed in figure 1B.

The topographic surface—represented by the upper model-layer—is considered to suffer no tensile stress, which is released by brittle fracturing at the main rift faults. The strain difference $\Delta\epsilon$ applied in equation (2) is therefore just the stretch of the lithosphere at the base of the boundary fault. We assume that tensile stress or strain decays with $1/R^2$, according to Saint-Venant's principle (Sadd, 2009; Wang and others, 2009). R is the distance to the main border fault. The tensile stress at a point in the lower slab is then given by

$$\epsilon = (x/l_0)^2 \cdot \epsilon_{max}. \qquad (2)$$

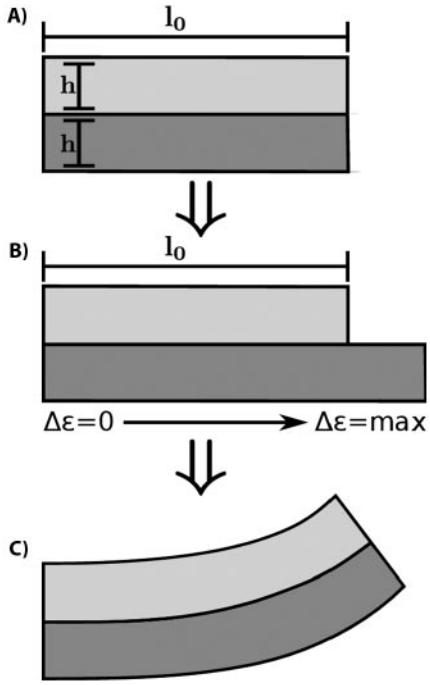

Fig. 10. Illustration of the beam model and the relevant parameters. (A) Two bonded layers with length l_0 and height h. (B) Extension of the lower layer creates a misfit strain $\Delta\epsilon$. The misfit strain increases from the left model boundary ($\Delta\epsilon$ = 0, onset of rift flank uplift) to the right boundary ($\Delta\epsilon$ = max, main rift boundary). The upper layer retains the initial length l_0. The height of each layer (h = 12.5 km) is half the total height of the boundary fault. (C) illustrates the resulting beam curvature.

l_0 is the distance between the onset of rift flank uplift and the main boundary fault of the rift and also the origin of the coordinate system (fig. 10). ϵ_{max} is the amount of extension exactly at the fault where the strain is maximum. ϵ_{max} is calculated from the total amount of extension as

$$\sum_i^n (\Delta l + \Delta l \cdot \epsilon_i) l_0 + l_0 \cdot \epsilon_{tot}. \quad (3)$$

Geophysical Significance

The rheology and the compensation of tensile strain in the crust are crucial parameters for the significance of the model. Since model layers have a finite thickness of 12.5 km, each layer represents a range of different viscosities and elastic moduli. The uppermost brittle and semi-brittle crust is subsumed into the viscosity of the upper model layer. We chose 100 GPa for the Young's modulus of the upper model layer and 180 GPa for the lower model layer (see Gölke and Mechie, 1994 and table 1). Strain rates, calculated from equation (2), are in a geologically realistic range (Hirth and Tullis, 1992; Behr and Platt, 2011). The maximum strain rate in immediate fault vicinity is 1.8×10^{-15} 1/s.

Among the parameters defining the Maxwell relaxation time, uncertainty of the Newtonian viscosity η is far larger than the uncertainty of the elastic modulus *E*. Estimates of the viscosity of the middle and the upper crust span several orders of magnitude, while estimates of the elastic moduli are less variable. Bills and others (1994), Gölke and Mechie (1994), and He and others (2011) give estimated viscosities within the upper 10 km of the crust ranging from 10^{21} Pa s to 10^{27} Pa s. In the depth

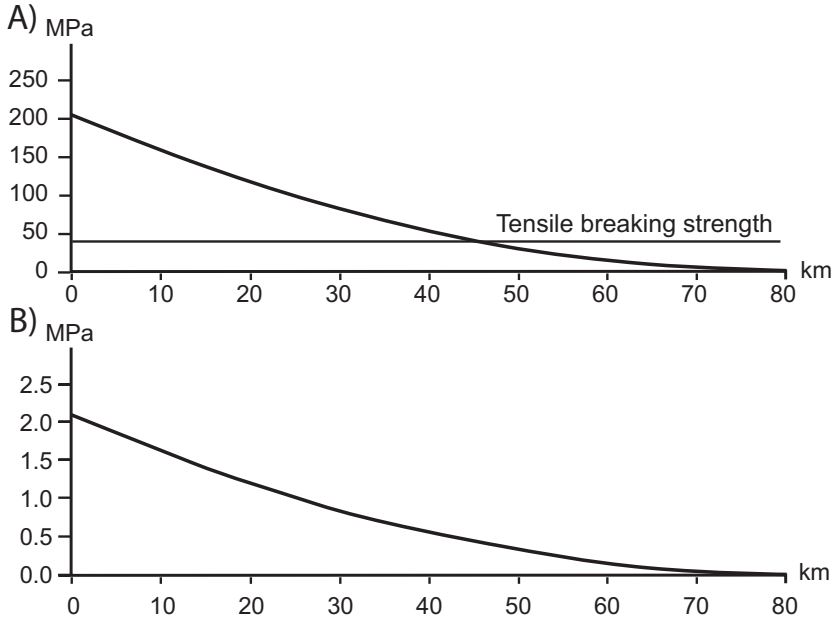

Fig. 11. Horizontal tensile stress calculated for the upper and lower crustal layer used in the beam bending experiments. Stress is calculated from the viscoelastic relaxation modulus and the local extension after 5 Ma with an extension rate of 2 mm/a, and assumes that yielding is exclusively ductile. (A) displays the stress in the upper model layer. Young's modulus is 100 GPa, viscosity is 10^{23} Pa s. The red horizontal line is the approximate tensile strength of crustal rocks (Kusznir and Park, 1982). Tensile stress is far larger than the crustal tensile brittle strength. (B) shows the tensile stress for the lower model layer, with 180 GPa and 3×10^{21} Pa s. Brittle fracturing does not occur in this layer.

range from 10 to 20 km, estimates of the Newtonian viscosity given by these authors range from 3×10^{20} Pa s to 3×10^{22} Pa s.

The first set of experiments described below is concerned with variations of the crustal viscosity and the calculation of the resulting surface. Based on these results and the corresponding discussion we identified a viscosity of 10^{23} Pa s for the upper model layer and of 3×10^{21} Pa s for the lower model layer as the most reasonable values, which were then inserted in the second set of experiments.

Figure 11 displays the lateral tensile stress (σ_x) within the upper and the lower model layer after 5 Ma, as a function of the distance from the main border fault. Viscosities of $3 \times 10^{21}/1 \times 10^{23}$ Pa s and Young's Moduli of 180/100 GPa are assumed for the lower and the upper layer, respectively. The values were estimated from the outcome of the first set of beam experiments discussed below.

The tensile stress shown in figure 11 is calculated from the cumulative relaxation modulus [eq (7) in the Appendix] and from the local lateral extension of the layer. The calculations assume hydrostatic ambient stress at this depth (Behr and Platt, 2011) and a Poisson ratio of 0.25—typical for crustal rocks (Gercek, 2007). Substituting the vertical strain ϵ_y by $\nu\epsilon_y$ in the equation for plane strain yields the tensile stress (eq 4).

$$\sigma_x = \frac{E(1-\nu)}{(1+\nu)(1-2\nu)}\,\epsilon_x + \frac{E\nu}{(1+\nu)*(1-2\nu)}\,\epsilon_y. \tag{4}$$

The crustal tensile strength is in the order of ~40 MPa (Kusznir and Park, 1982). The maximum tensile stress in the lower model layer in immediate fault vicinity is ~2.1

MPa. We can thus infer that brittle fracturing does not occur within the lower model layer and stress is compensated by ductile creep alone.

Within the upper layer, the maximum tensile stress reaches ~0.2 GPa, and lateral tensile stress has led to brittle failure. This is in agreement with the basic assumption that tensile stress in the upper layer does not exist. The misfit stress between upper and lower layer is therefore defined by the ductile yielding of the lower layer alone.

RESULTS AND DISCUSSION

First Set of Experiments: Variations of Crustal Viscosity

The first set of experiments dealt with parameter variations of the crustal viscosity and the calculation of the resulting surface topography. The primary aim of these experiments was to determine whether the rift flank topography found in the Albertine Rift can be generated on the basis of reasonable crustal viscosities.

Parameters used for the upper model layer were specified in advance as 10^{23} Pa s, 10^{24} Pa s, and 10^{25}. The viscosity of the lower layer was varied until the model produced a topography, which fitted the topographic profile of a rift flank in the Rwenzori region, shown in figure 1B. From these simulations we found the following fitting parameter pairs for the upper/lower model layer: 10^{23} Pa s/3×10^{21} Pa s, 10^{24} Pa s/10^{22} Pa s, 10^{25} Pa s/6×10^{22} Pa s.

A value of 6×10^{22} Pa s for the viscosity of the lower model layer is higher than the estimates cited above and was thus neglected. A viscosity of 10^{22} Pa s, resulting from an upper layer viscosity of 10^{24} Pa s, is at the upper limit of possible values and seems therefore unreasonable, in particular if we consider that a single model layer represents a variety of parameters. This means that the best fitting viscosities for the upper model layer is 10^{23} Pa s and 3×10^{21} for the lower model layer, which were used in the second set of experiments.

The results are summarized in figure 12A, where the topography generated by these parameter pairs is compared with the topographic profile from the lake Albert Rift flank.

Second Set of Experiments: Variations of the Extension Rate

In the second set of experiments we tested the relation between the rate of continental extension and the resulting flank uplift. The experimental setup was generally identical to the experiments described above. As a consequence of the results and the discussion of the previous set of experiments, the viscosity of the upper/lower model layer was set to 10^{23} Pa s and to 3×10^{21} Pa s respectively. The different topographies that arise from the different rates of extension are displayed in figure 12B.

Higher strain rates result in a higher uplift of the rift flanks, caused by an increase of the relaxation modulus E_{rel} defined in equation (6). If the strain rate is successively increased it can be observed that rift flank uplift converges towards a limit, which thus defines the maximum possible uplift of a particular crustal rheology. In the given setup this limit is at about 3500 m. Thus, strain rates larger than approximately 20 mm/a do not result in a relevant increase of the rift flank topography.

If the extension is interrupted and the strain rate drops to zero, complete viscoelastic relaxation of the crust can occur and the model rift flanks subside back to continental surface level within a few 10000 years.

CONCLUSION

Our numerical experiments indicate that a significant part of the driving force behind the uplift of the Rwenzori horst results from the difference of the tensile lateral stress between upper and lower crust. The stress difference is caused by different yield

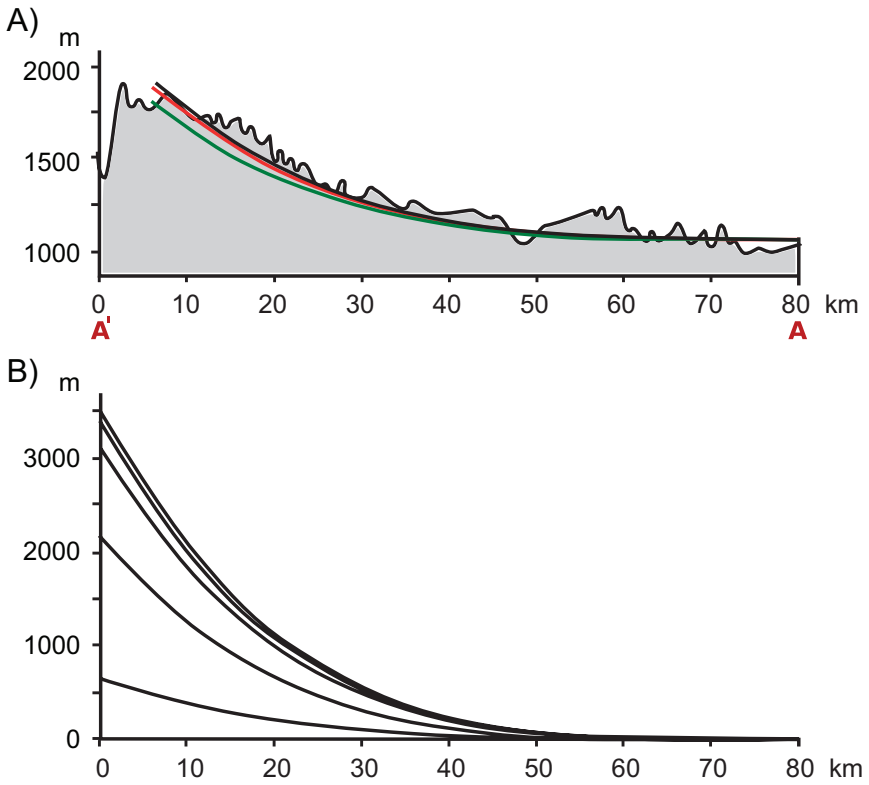

Fig. 12. Topographic uplift resulting from crustal bending. Uplift is plotted against the distance from the main boundary fault of the rift. (A) uplift resulting for three different viscosity combinations of the upper/lower model layer, compared to the topographic profile from the Rwenzori region shown in figure 1B. Upper/lower crustal layer: Red line: $10^{24}/10^{22}$ Pa s; green line: $10^{25}/6 \times 10^{22}$ Pa s; black lines: $10^{23}/3 \times 10^{21}$ Pa s. The height of the boundary fault is 25 km. All other parameters: see text. Note that the model topography closely resembles the peculiar shape of the rift flank topography. (B) shows the topography resulting from viscosities upper/lower layer of $10^{23}/3 \times 10^{21}$ Pa s and a number of different tensile strain rates. The strain rates are, from the lowest to highest uplift (mm/a): 2, 10, 20, 30, 40. The uplift converges against a maximum value for large strain rates, here ~4.5 km.

mechanisms in the upper and the lower crust. The amount of uplift is strongly influenced by the stiffness of the horst block. A weak horst bends, contains two rift flanks and does not show a Moho uplift. A stiff horst increases the topographic uplift significantly and also leads to a high Moho below the horst.

Results of both, lattice particle simulations and numerical beam bending experiments, indicate that the model is in agreement with seismological observations in the Rwenzori region. The Rwenzori block is stiff, is surrounded by steep non-listric faults and the Moho below the horst is high. Therefore the two rift segments that surround the Rwenzori horst behave as one large rift with the horst sitting at the highest point of elevation. Our lattice-particle simulation show that uplift of the central horst of up to 2500 m above the African Plateau is realistic with the current extension rate of 2 mm/a. In addition numerical beam bending models indicate that the uplift increases with increasing extension rate. Our models are currently not able explain the total Rwenzori elevation so that an additional isostatic force or 3D effect due to horst rotation and shearing is probable.

ACKNOWLEDGMENTS

We acknowledge funding of our research by DFG grant KO 2463/4-2 of the Forschergruppe "Rift Dynamics, uplift and climate change in Equatorial Africa." We also thank the reviewers for their comments and suggestions, which helped to improve the manuscript.

Appendix

Governing equations used in beam calculations

The curvature κ of a two-layer composite with a strain difference $\Delta\epsilon$ can be calculated by the following equation:

$$\kappa = \frac{12E_1E_2 \cdot \Delta\epsilon}{h(E_1^2 + E_2^2 + 14E_1E_2)}, \tag{5}$$

which is an adaption of equation (7) in the article by Clyne (1996) for the case of two layers with equal thickness h. $E_{1/2}$ is the Young's modulus of the respective layers. Figure 10 illustrates the concept for the case of horizontal extension, where the upper layer is not stretched.

The scheme is adapted to viscoelastic material behavior by replacing the Young's modulus E of the respective layers with the viscoelastic relaxation modulus

$$E_{rel} := E \cdot exp(-t/\tau). \tag{6}$$

$\tau := \eta/E$ is the Maxwell relaxation time (Roylance, 2001), and η the viscosity. This particular formulation of the relaxation modulus is true if the strain is constant.

Using equation (2), E_{rel} for a constant strain rate ϵ after n time steps Δt can be calculate by an appropriate update scheme (O'Brien, 2008). For our purpose that is:

$$E_{rel} = \frac{\sum_{i=1}^{n} E \cdot exp(-i\Delta t/\tau)}{n}. \tag{7}$$

The local curvature of the topography—and, consequently, the local inclination and thus the actual uplift—increases with proximity to the main rift fault. Thus it must be assumed that the strain difference between the layers decreases with increasing distance from the main rift fault, until the point where the crust is not stretched at all. Therefore the computer experiments require a scheme to calculate the local crustal strain as a function of the distance from the rift fault. Since extension of rift systems is usually given as the total amount of extension, the scheme has to satisfy the condition:

$$\epsilon_{tot} = \int_0^{x_0} \epsilon(x)\,dx, \tag{8}$$

where x_0 is the distance from the main rift fault where lithospheric curvature vanishes.

The local curvature is calculated for m intervals with length Δl of the composite beam, starting from the point of the onset of rift flank uplift. The curvature of each interval is transformed into a tangent line and the slope of each interval results from the sum of the local tangent and the tangents to the previous intervals. The number of intervals is increased until convergence occurs. This numerical scheme, where the topography is successively calculated from the local slope of the surface, is comparable to an explicit Euler forward method.

References

Allen, D. N. de G., 1954, Relaxation Methods: New York/Toronto/London, McGraw-Hill Books, 257 p.

Bahat, D., and Paul, M., 1987, Horst faulting in continental rifts: Tectonophysics, v. 141, n. 1–3, p. 61–73, http://dx.doi.org/10.1016/0040-1951(87)90174-0

Bauer, F. U., Glasmacher, U. A., Ring, U., Schumann, A., and Nagudi, B., 2010, Thermal and exhumation history of the central Rwenzori Mountains, Western Rift of the East African Rift System, Uganda: International Journal of Earth Sciences, v. 99, n. 7, p. 1575–1597, http://dx.doi.org/10.1007/s00531-010-0549-7

Bauer, F. U., Karl, M., Glasmacher, U. A., Nagudi, B., Schumann, A., and Mroszewski, L., 2012, The Rwenzori Mountains of western Uganda—Aspects on the evolution of their remarkable morphology within the Albertine Rift: Journal of African Earth Sciences, v. 73–74, p. 44–56, http://dx.doi.org/10.1016/j.jafrearsci.2012.07.001

Behr, W. M., and Platt, J. P., 2011, A naturally constrained stress profile through the middle crust in an

extensional terrane: Earth and Planetary Science Letters, v. 303, n. 3–4, p. 181–192, http://dx.doi.org/10.1016/j.epsl.2010.11.044

Bills, B. G., Currey, D. R., and Marshall, G. A., 1994, Viscosity estimates for the crust and upper mantle from patterns of lacustrine shoreline deformation in the Eastern Great Basin: Journal of Geophysical Research, v. 99, n. B11, p. 22059–22086, http://dx.doi.org/10.1029/94JB01192

Bott, M. H. P., 1976, Formation of sedimentary basins of graben type by extension of the continental crust: Tectonophysics, v. 36, n. 1–3, p. 77–86, http://dx.doi.org/10.1016/0040-1951(76)90007-X

Buck, W. R., 1988, Flexural rotation of normal faults: Tectonics, v. 7, n. 5, p. 959–973, http://dx.doi.org/10.1029/TC007i005p00959

——— 1991, Modes of continental lithospheric extension: Journal of Geophysical Research, v. 96, n. B12, p. 20161–20178, http://dx.doi.org/10.1029/91JB01485

Cai, M., 2009, Practical estimates of tensile strength and Hoek-Brown strength parameter m_i of brittle rocks: Rock Mechanics and Rock Engineering, v. 43, n. 2, p. 167–184, http://dx.doi.org/10.1007/s00603-009-0053-1

Chorowicz, J., 2005, The East African rift system: Journal of African Earth Sciences, v. 43, n. 1–3, p. 379–410, http://dx.doi.org/10.1016/j.jafrearsci.2005.07.019

Clyne, T., 1996, Residual stresses in surface coatings and their effects on interfacial debonding: Key Engineering Materials, v. 117, p. 307–330, http://dx.doi.org/10.4028/www.scientific.net/KEM.116-117.307

Ebinger, C. J., 1989, Tectonic development of the western branch of the East African rift system: Geological Society of America Bulletin, v. 101, n. 7, p. 885–903, http://dx.doi.org/10.1130/0016-7606(1989)101⟨0885:TDOTWB⟩2.3.CO;2

Ebinger, C. J., Bechtel, T. D., Forsyth, D. W., and Bowin, C. O., 1989, Effective elastic plate thickness beneath the east African and Afar plateaus and dynamic compensation of the uplifts: Journal of Geophysical Research, v. 94, n. B3, p. 2883–2901, http://dx.doi.org/10.1029/JB094iB03p02883

Gercek, H., 2007, Poisson's ratio values for rocks: International Journal of Rock Mechanics and Mining Sciences, v. 44, n. 1, p. 1–13, http://dx.doi.org/10.1016/j.ijrmms.2006.04.011

Gölke, M., and Mechie, J., 1994, Finite-element modelling of the structure and evolution of the South Kenya Rift, East Africa: Tectonophysics, v. 236, n. 1–4, p. 439–452, http://dx.doi.org/10.1016/0040-1951(94)90188-0

Häuserer, M., ms, 2010, Magnetotellurik in der Rwenzori Region im Westen Ugandas: Ein anisotropes 3D Modell: Frankfurt, Germany, Universität Frankfurt, Ph. D. thesis, 130 p.

He, J., Xia, W., Lu, S., and Qian, H., 2011, Three-dimensional finite element modeling of stress evolution around the Xiaojiang fault system in the southeastern Tibetan plateau during the past ~500 years: Tectonophysics, v. 507, n. 1–4, p. 70–85, http://dx.doi.org/10.1016/j.tecto.2011.05.009

Hirth, G., and Tullis, J., 1992, Dislocation creep regimes in quartz aggregates: Journal of Structural Geology, v. 14, n. 2, p. 145–159, http://dx.doi.org/10.1016/0191-8141(92)90053-Y

Jiang, H., and Xie, Y., 2011, A note on the Mohr–Coulomb and Drucker–Prager strength criteria: Mechanics Research Communications, v. 38, n. 4, p. 309–314, http://dx.doi.org/10.1016/j.mechrescom.2011.04.001

Karner, G. D., Byamungu, B. R., Ebinger, C. J., Kampunzu, A. B., Mukasa, R. K., Nyakaana, J., and Upcott, N. M., 2000, Distribution of crustal extension and regional basin architecture of the Albertine rift system, East Africa: Marine and Petroleum Geology, v. 17, n. 10, p. 1131–1150, http://dx.doi.org/10.1016/S0264-8172(00)00058-1

Koehn, D., Malthe-Sorenssen, A., and Passchier, C. W., 2006, The structure of reactive grain-boundaries under stress containing confined fluids: Chemical Geology, v. 230, n. 3–4, p. 207–219, http://dx.doi.org/10.1016/j.chemgeo.2006.02.026

Koehn, D., Aanyu, K., Haines, S., and Sachau, T., 2008, Rift nucleation, rift propagation and the creation of basement micro-plates within active rifts: Tectonophysics, v. 458, n. 1–4, p. 105–116, http://dx.doi.org/10.1016/j.tecto.2007.10.003

Koehn, D., Lindenfeld, M., Rümpker, G., Aanyu, K., Haines, S., Passchier, C. W., and Sachau, T., 2010, Active transsection faults in rift transfer zones: evidence for complex stress fields and implications for crustal fragmentation processes in the western branch of the East African Rift: International Journal of Earth Sciences, v. 99, n. 7, p. 1633–1642, http://dx.doi.org/10.1007/s00531-010-0525-2

Kusznir, N., and Ziegler, P., 1992, The mechanics of continental extension and sedimentary basin formation: A simple-shear/pure-shear flexural cantilever model: Tectonophysics, v. 215, n. 1–2, p. 117–131, http://dx.doi.org/10.1016/0040-1951(92)90077-J

Kusznir, N. J., and Park, R. G., 1982, Intraplate lithosphere strength and heat flow: Nature, v. 299, p. 540–542, http://dx.doi.org/10.1038/299540a0

Kusznir, N. J., Vita-Finzi, C., Whitmarsh, R. B., England, P., Bott, M. H. P., Govers, R., Cartwright, J., and Murrell, S., 1991, The Distribution of Stress with Depth in the Lithosphere: Thermo-Rheological and Geodynamic Constraints [and Discussion]: Philosophical Transactions of the Royal Society of London, Series A: Physical and Engineering Sciences, v. 337, p. 95, http://dx.doi.org/10.1098/rsta.1991.0109

Li, Q., Liu, M., and Zhang, H., 2009, A 3-D viscoelastoplastic model for simulating long-term slip on non-planar faults: Geophysical Journal International, v. 176, n. 1, p. 293–306, http://dx.doi.org/10.1111/j.1365-246X.2008.03962.x

Lindenfeld, M., and Rümpker, G., 2011, Detection of mantle earthquakes beneath the East African Rift: Geophysical Journal International, v. 186, n. 1, p. 1–5, http://dx.doi.org/10.1111/j.1365-246X.2011.05048.x

Lindenfeld, M., Rümpker, G., Link, K., Koehn, D., and Batte, A., 2012, Fluid-triggered earthquake swarms in the Rwenzori region, East African Rift—Evidence for rift initiation: Tectonophysics, v. 566–567, p. 95–104, http://dx.doi.org/10.1016/j.tecto.2012.07.010

Link, K., Koehn, D., Barth, M. G., Tiberindwa, J. V., Barifaijo, E., Aanyu, K., and Foley, S. F., 2010, Continuous cratonic crust between the Congo and Tanzania blocks in western Uganda: International Journal of Earth Sciences, v. 99, n. 7, p. 1559–1573, http://dx.doi.org/10.1007/s00531-010-0548-8

Malthe-Sørenssen, A., Walmann, T., Feder, J., Jøssang, T., Meakin, P., and Hardy, H. H., 1998, Simulation of extensional clay fractures: Physical Review E, v. 58, n. 5, p. 5548–5564, http://dx.doi.org/10.1103/PhysRevE.58.5548

McConnell, R. B., 1972, Geological development of the rift system of eastern Africa: Geological Society of America Bulletin, v. 83, n. 9, p. 2549–2572, http://dx.doi.org/10.1130/0016-7606(1972)83[2549:GDOTRS]2.0.CO;2

McKenzie, D., 1978, Some remarks on the development of sedimentary basins: Earth and Planetary Science Letters, v. 40, n. 1, p. 25–32, http://dx.doi.org/10.1016/0012-821X(78)90071-7

Morley, C. K., Nelson, R. R., Patton, T. L., and Munn, S. C., 1990, Transfer zones in the East African Rift System and their relevance to hydrocarbon exploration in rifts (1): AAPG Bulletin, v. 74, p. 1234–1253.

O'Brien, G. S., 2008, Discrete visco-elastic lattice methods for seismic wave propagation: Geophysical Research Letters, v. 35, n. 2, http://dx.doi.org/10.1029/2007GL032214

Palmström, A., and Singh, R., 2001, The deformation modulus of rock masses—comparisons between in situ tests and indirect estimates: Tunnelling and Underground Space Technology, v. 16, n. 2, p. 115–131, http://dx.doi.org/10.1016/S0886-7798(01)00038-4

Parsons, T., 2006, The Basin and Range Province, *in* Olsen, K., editor, Continental rifts: evolution, structure, tectonics: Elsevier, Developments in Geotectonics, v. 25, p. 277–324, http://dx.doi.org/10.1016/S0419-0254(06)80015-7

Pickford, M., Sneut, B., and Hadoto, D., 1993, Geology and palaeobiology of the Albertine Rift Valley Uganda-Zaire, v. 1: Geology: CIFEG Occasional Publications, v. 24, p. 1–190.

Ring, U., 2008, Extreme uplift of the Rwenzori Mountains in the East African Rift, Uganda: Structural framework and possible role of glaciations: Tectonics, v. 27, n. 4, TC4018, http://dx.doi.org/10.1029/2007TC002176

Roller, S., Hornung, J., Hinderer, M., and Ssemmanda, I., 2010, Middle Miocene to Pleistocene sedimentary record of rift evolution in the southern Albert Rift (Uganda): International Journal of Earth Sciences, v. 99, n. 7, p. 1643–1661, http://dx.doi.org/10.1007/s00531-010-0560-z

Royden, L., and Keen, C. E., 1980, Rifting process and thermal evolution of the continental margin of Eastern Canada determined from subsidence curves: Earth and Planetary Science Letters, v. 51, n. 2, p. 343–361, http://dx.doi.org/10.1016/0012-821X(80)90216-2

Roylance, D., 2001, Engineering viscoelasticity: URL http://web.mit.edu/course/3/3.11/www/modules/visco.pdf

Sachau, T., and Koehn, D., 2010, Faulting of the lithosphere during extension and related rift-flank uplift: a numerical study: International Journal of Earth Sciences, v. 99, n. 7, p. 1619–1632, http://dx.doi.org/10.1007/s00531-010-0513-6

——— 2012, "Melange": A viscoelastic lattice-particle model applicable to the lithosphere: Geochemistry Geophysics Geosystems, v. 13, n. 12, Q12009, http://dx.doi.org/10.1029/2012GC004452

Sachau, T., Koehn, D., and Passchier, C., 2011, Lattice-particle simulation of stress patterns in a Rwenzori-type rift transfer zone: Journal of African Earth Sciences, v. 61, n. 4, p. 286–295, http://dx.doi.org/10.1016/j.jafrearsci.2011.08.006

Sadd, M., 2005, Elasticity: Theory, Applications, and Numerics: Amsterdam, Academic Press, 387 p.

——— 2009, Elasticity: Theory, Applications, and Numerics: Amsterdam, Academic Press, 552 p.

Schlueter, T., 1997, Structural evolution of the East African Rift System, *in* Bender, F., Jacobshagen, V., and Luettig, G., editors, Beiträge zur Regionalen Geologie der Erde, band 27: Berlin, Stuttgart, Gebrueder Bornträger, p. 265–301.

Stamps, D. S., Calais, E., Saria, E., Hartnady, C., Nocquet, J.-M., Ebinger, C. J., and Fernandes, R. M., 2008, A kinematic model for the East African Rift: Geophysical Research Letters, v. 35, n. 5, L05304, http://dx.doi.org/10.1029/2007GL032781

Upcott, N. M., Mukasa, R. K., Ebinger, C. J., and Karner, G. D., 1996, Along-axis segmentation and isostasy in the Western rift, East Africa: Journal of Geophysical Research, v. 101, n. B1, p. 3247–3268, http://dx.doi.org/10.1029/95JB01480

Wallner, H., and Schmeling, H., 2010, Rift induced delamination of mantle lithosphere and crustal uplift: a new mechanism for explaining Rwenzori Mountains' extreme elevation?: International Journal of Earth Sciences, v. 99, n. 7, p. 1511–1524, http://dx.doi.org/10.1007/s00531-010-0521-6

Wang, N., Tytell, J. D., and Ingber, D. E., 2009, Mechanotransduction at a distance: mechanically coupling the extracellular matrix with the nucleus: Nature Reviews Molecular Cell Biology, v. 10, p. 75–82, http://dx.doi.org/10.1038/nrm2594

Wölbern, I., Rümpker, G., Schumann, A., and Muwanga, A., 2010, Crustal thinning beneath the Rwenzori region, Albertine rift, Uganda, from receiver-function analysis: International Journal of Earth Sciences, v. 99, n. 7, p. 1545–1557, http://dx.doi.org/10.1007/s00531-009-0509-2

Wölbern, I., Rümpker, G., Link, K., and Sodoudi, F., 2012, Melt infiltration of the lower lithosphere beneath the Tanzania craton and the Albertine rift inferred from S receiver functions: Geochemistry, Geophysics, Geosystems, v. 13, n. 8, http://dx.doi.org/10.1029/2012GC004167

Wolde Gabriel, G., Yemane, T., Suwa, G., White, T., and Asfaw, B., 1991, Age of volcanism and rifting in the Burji-Soyoma area, Amaro Horst, southern Main Ethiopian Rift: geo- and biochronologic data: Journal of African Earth Sciences (and the Middle East), v. 13, n. 3–4, p. 437–447, http://dx.doi.org/10.1016/0899-5362(91)90107-A